RSC Advances

PAPER

View Article Online
View Journal | View Issue

Cite this: *RSC Adv.*, 2015, **5**, 8323

Improved photocatalytic activity of g-C_3N_4 derived from cyanamide–urea solution†

Xiangqian Fan,[a] Zheng Xing,[b] Zhu Shu,[c] Lingxia Zhang,*[a] Lianzhou Wang[b] and Jianlin Shi*[a]

Received 14th December 2014
Accepted 24th December 2014

DOI: 10.1039/c4ra16362a

www.rsc.org/advances

This paper describes the fabrication of g-C_3N_4 by the polymerization of cyanamide–urea solution at elevated temperatures. The textural properties and electronic band structure of the obtained g-C_3N_4 were investigated in detail. The photocatalytic activity for both oxidative and reductive reactions of the as-synthesized g-C_3N_4 was found to be enhanced as the polymerization temperature increase and the g-C_3N_4 obtained at 700 °C (CN-700) showed the best photocatalytic activity under visible-light (λ > 420 nm). Considering that the rather wide band gap (3.01 eV) of CN-700 disables the electron transition from the valence band to the conduction band by visible light (λ > 420 nm), it is believed the n–π^* transition, which is alternatively proposed in this study, plays a key role in its photocatalytic activity. In light of this discovery, the variation of the electron-transition mechanism for g-C_3N_4 fabricated at different polymerization temperatures has been firstly investigated.

1. Introduction

Searching for applicable semiconductors for splitting water to produce hydrogen and photocatalytic degradation of organic pollutants has now attracted worldwide attention because of increasingly severe energy shortage and environment pollution.[1,2] In addition to suitable band edges, an excellent photocatalyst should possess several other characteristics such as visible light response, good stability, environmental friendliness and low cost, *etc.* Among numerous photocatalysts, g-C_3N_4, which has been successfully developed to split water and degrade pollutants recently, features all of the above characteristics, making it a promising candidate for practical application.[3–5] However, the photocatalytic efficiency of g-C_3N_4 is still far from satisfactory because of its uncompetitive band levels (top level of valence band and bottom level of conduction band) and high recombination rate of photo-generated charge carriers predominantly limit its photo-oxidation or photo-reduction ability and the amount of charge carries involved in photocatalytic reactions, respectively. Generally, g-C_3N_4 is synthesized by thermal polymerization of precursors such as cyanamide, dicyanodiamide, melamine, *etc.*[6–8] Its band levels can be optimized by several strategies like increasing the polymerization temperature,[9] heteroatom doping,[10] secondary thermal oxidation[11] and liquid-exfoliation into nanosheets[12] *etc.* Obviously, temperature regulation is the simplest method. Moreover, increasing the polymerization temperature can also improve the crystallinity of g-C_3N_4, which is beneficial for the separation and migration of photogenerated charge carriers.[1] Unfortunately, g-C_3N_4 derived from almost all kinds of precursors decomposes vigorously at above 650 °C. Therefore, in order to further optimize the band levels and crystallinity of g-C_3N_4 by simply increasing the polymerization temperature, it is the only way to substantially improve its thermal stability at elevated temperatures. Additionally, though the relationship between the structure and polymerization temperature of g-C_3N_4 and how its structure influences the photocatalytic performance have been reported,[8,9] they are still rough and more details are necessary to be understood.

In order to improve the thermal stability of g-C_3N_4, in this work, a new kind of liquid precursor composed of cyanamide and urea with a mass ratio of 2 : 1 has been adopted. Cyanamide and urea can be pyrolyzed into melamine and cyanuric acid at increased temperatures, respectively,[6,13] and these two intermediates tend to form melamine–cyanuric acid (MCA) complex through triple hydrogen bond (Fig. S1†).[14] It should be mentioned that, since cyanamide and urea are mutually soluble, thus the MCA formed by these two intermediates (melamine and cyanuric acid) through triple hydrogen bond are much more homogeneous at molecular level, in contrast to the traditional MCA formed by externally/separately introduced and mechanically mixed melamine and cyanuric acid.[15] It can be

[a]*State Key Laboratory of High Performance Ceramics and Superfine Microstructure, Shanghai Institute of Ceramics, Chinese Academy of Sciences, Shanghai 20050, PR China. E-mail: zhlingxia@mail.sic.ac.cn; jlshi@mail.sic.ac.cn; Tel: +86 021 52413122; +86 021 52413903*

[b]*ARC Centre of Excellence for Functional Nanomaterials, School of Chemical Engineering, The University of Queensland, Brisbane, QLD 4072, Australia*

[c]*Faculty of Material Science and Chemistry, China University of Geosciences, Wuhan 430074, PR China*

† Electronic supplementary information (ESI) available. See DOI: 10.1039/c4ra16362a

predicted that these hydrogen bonds to some extent could prevent the thermal volatilization of these intermediates and help solidify/extend the carbon nitride networks during polymerization, thus the thermal stability of g-C_3N_4 could be enhanced and the synthesis of g-C_3N_4 at higher temperatures would be feasible. Actually, the yield of g-C_3N_4 synthesized using this liquid precursor was considerably high even at 700 °C (Table S1†). As far as we know, this is the highest temperature that g-C_3N_4 can withstand without drastic structure decomposition. In comparison, the traditional g-C_3N_4 obtained from pure cyanamide would violently decompose at 600 °C.

2. Material and methods

2.1 Synthesis procedure

In a typical synthesis procedure, a certain amount of mixture consisting of 5 g cyanamide and 2.5 g urea (with a mass ratio of 1 : 0.5) was melted at 70 °C, stirred for about 10 min in a crucible with a cover, and then heated to a certain temperature in a muffle furnace for 4 h at a heating rate of 2 °C min^{-1}. The g-C_3N_4 samples prepared at different temperatures were ground and denoted as CN-*T* (*T*/°C = 500, 550, 600, 650 and 700). For comparison, the traditional g-C_3N_4 was synthesized by the polymerization of cyanamide at 550 °C.

2.2 Characterization

The X-ray diffraction (XRD) patterns were recorded on a Rigaku D/Max-2200 PC diffractometer with Cu Kα radiation. The surface area of each sample was calculated by the Brunauer–Emmett–Teller (BET) method from the adsorption data obtained on a Micromeritics Tristar 3020 system. Fourier transform infrared (FT-IR) spectra were obtained with Nicolet iS10 FTIR spectrometer. X-Ray photoelectron spectroscopy (XPS) measurements were carried out on a Thermo Scientific ESCALAB 250 spectrometer with Al Kα radiation as the excitation source. Binding energies for the high resolution spectra were calibrated by setting C 1s to 284.8 eV. Elemental analysis (C, H, N) was taken on VARIO EL III microanalyzer. UV-vis diffuse reflectance spectra were performed on a Shimadzu UV-3600 system. Photoluminescence (PL) spectra were performed on a Shimadzu RF-5301 spectrometer (excitation wavelength = 330 nm). Time-resolved fluorescence emission spectra were recorded at room temperature with a Fluorescence spectrophotometer (Edinburgh Instruments, FLSP-920) monitored at 470 nm (excitation wavelength = 330 nm). The transmission electron microscope (TEM) images were obtained on a transmission electron microscope (FEI Tecnai-G2 F20) and scanning electron microscopy (SEM) images were obtained on a field emission scanning electron microscope (Hitachi S-4800).

2.3 Photocatalytic degradation of RhB

The photooxdation activities of the obtained samples were evaluated *via* the photocatalytic degradation of RhB in an aqueous solution under visible light irradiation. A 300 W Xe lamp equipped with an optical cut-off filter (λ > 420 nm) was chosen as the visible light source. 0.1 g of photocatalyst was suspended in 100 mL of 10 mg L^{-1} RhB aqueous solution in a container. The suspensions were stirred in the dark to establish an adsorption–desorption equilibrium before irradiation. During the photodegradation, about 3 mL of the suspension was collected at an interval of 5 min. After filtration, the solution was detected by a Hitachi U-3310 UV-visible spectrophotometer.

2.4 Photocatalytic H_2 evolution

The photocatalytic H_2 evolution reactions were carried out in a quartz reaction vessel connected to a closed gas circulation and evacuation system. 0.1 g catalyst was suspended in 100 mL aqueous solution containing triethanolamine (10 vol%) as the sacrificial electron donor. 3 wt% Pt was loaded on the surface of the carbon nitride catalyst by an *in situ* photodeposition method using H_2PtCl_6 as precursor. The suspension was thoroughly degassed and irradiated by a 300 W Xe lamp equipped with an optical cut-off filter (λ > 420 nm) to eliminate ultraviolet light. The temperature of the reactant solution was maintained at 293 K by a flow of cooling water during the reaction. The evolved gas was analyzed every 1 h by gas chromatography equipped with a thermal conductive detector. After reaction for 4 h, the system was evacuated again. This process repeated 3 times (*i.e.* a 12 h recycling experiment with intermittent evacuation every 4 h).

3. Results and discussion

The XRD patterns in Fig. 1a reveal the typical graphite-like structure of all the samples. Take the g-C_3N_4 obtained at 500 °C (CN-500) for example, the distinct peak at 27.4° belongs to the characteristic (002) interlayer-stacking reflection of aromatic systems, while the other pronounced peak at 13.1° which can be indexed as (100) plane represents the in-plane structural packing motif.[16] As can be clearly seen in Fig. 1a, the (002) peak of g-C_3N_4 becomes sharpened gradually as the temperature increases from 500 to 700 °C, indicating the promoted polymerization degree of interlayer networks of g-C_3N_4 and more complete crystallization at the elevated temperatures. The location of these two peaks also changes with the increase of temperature. The (100) peak down-shifts from 13.08° to 12.78° (enlarged image is given in Fig. S2†), corresponding to an increase of the in-planar hole-to-hole distance from 0.676 to 0.692 nm, which is ascribed to the promoted planarization of g-C_3N_4 layers. The (002) peak up-shifts from 27.38 to 27.94° as temperature increases from 500 to 700 °C, and the corresponding interlayer distance decreases from 0.326 to 0.319 nm, indicating the gradual structural compaction of g-C_3N_4. This is because the promoted planarization of g-C_3N_4 layers is beneficial for π electron delocalization, thus strengths the π–π stacking interactions of interlayers and leads to a decreased interlayer distance. It is worth noticing that the interlayer distance of CN-700 (0.319 nm) is the smallest one ever found for the stacking of aromatic units.[17]

The FT-IR spectra of all the samples are shown in Fig. 1b. The most intense band at 809 cm^{-1} represents the out-of-plane bending vibration of tri-*s*-triazine rings. And several strong

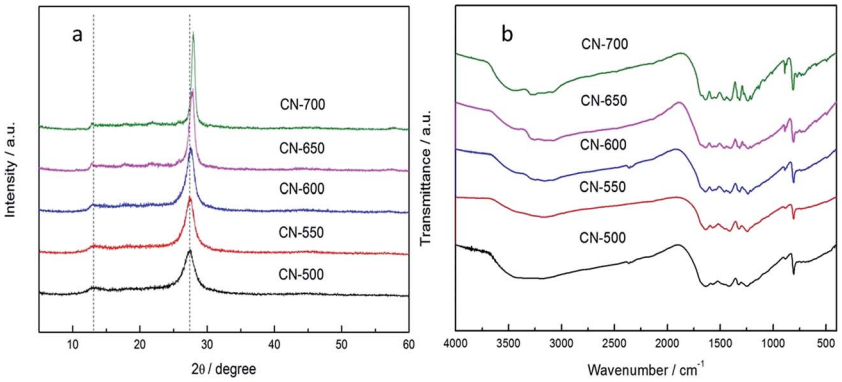

Fig. 1 (a) XRD patterns and (b) FT-IR spectra of g-C_3N_4 samples prepared at different temperatures.

bands at 1200–1650 cm^{-1}correspond to the typical stretching modes of C–N heterocycles. The broad bands at about 3000–3500 cm^{-1} are due to stretching vibrations of –NH, which originates from the terminal amino groups in the g-C_3N_4 structure. As discussed above, increasing the polymerization temperature can promote the planarization of g-C_3N_4 layers, which would weaken the interactions between the two neighboring atoms separately located in two adjacent tri-*s*-triazine rings. Consequently, these atoms would vibrate more vigorously because of less constraint, which can be well confirmed by the FT-IR spectra of g-C_3N_4, where all vibration bands become better distinguished with the increase of polymerization temperature. The chemical composition and C/N ratios for all the samples are shown in Table S1.† The C/N ratio of g-C_3N_4 increases with the elevation of condensation temperature, but all are below 0.75 of the ideal crystallized g-C_3N_4, implying the incomplete condensation of the obtained g-C_3N_4.[18]

XPS spectroscopy was further used to investigate the chemical and structure information of the as-synthesized g-C_3N_4. As shown in Fig. S3,† three signals belonging to C, N and O can be found. The corresponding high resolution spectra of C1s, N1s and O1s are also given. The C1s spectra can be fitted with three peaks centered at 284.8, 286.3 and 288.0 eV, which are attributed to sp^2 C–C bonds, C–O bonds in carbon species and sp^2 bonded carbon (N–C═N) in N-containing aromatic rings, respectively. The N1s spectrum can be deconvoluted into four peaks. The main peak at 398.6 eV is assigned to sp^2 nitrogen (C═N–C) involved in triazine rings, while the peak at 399.9 eV originates from the tertiary nitrogen bonded to carbon atoms in the form of N–(C)3. The peak at 401.2 eV is ascribed to amino functions (C–N–H). Another peak centered at 404.2 eV is associated to charging effects or positive charge localization in heterocycles. In addition, the peak of O1s spectrum at 532.2 eV is assigned to O–C group, which originates from the adsorbed oxygen species.[7]

Based on the traditional mechanism of the formation of g-C_3N_4, combined with the above structural and compositional characterizations of the as-synthesized g-C_3N_4, a possible reaction path of our strategy is proposed in Scheme S1.† Firstly, the pyrolysis of cyanamide and urea leads to the formation of melamine and cyanuric acid, respectively. Then cyanuric acid reacts with NH_3 generated during various pyrolysis reactions and concentrated in the covered crucible, to form melamine. Finally, melamine polymerizes to g-C_3N_4.

The optical properties of g-C_3N_4 samples obtained at different temperatures were examined by UV-vis diffuse reflectance spectroscopy. It can be seen in Fig. 2a that all samples exhibit typical semiconductor absorption characteristics. Their intrinsic absorption edges and corresponding estimated band gap energy values (Table S2†) vary with polymerization temperatures. At the very beginning, increasing the temperature from 500 °C to 600 °C induces the gradual decrease of band gap from 2.74 eV to 2.65 eV, owing to the improved polymerization degree with the extended electron delocalization in aromatic layers at higher temperatures. However, as the temperature further increases from 600 °C to 700 °C, the band gap energy exhibits an enhancement from 2.65 eV to 3.01 eV. This blue-shift results from the decrease of orbital conjugation degree of g-C_3N_4. There is no doubt that the amount of tri-*s*-triazine rings in g-C_3N_4 layers contributes to the electron delocalization of g-C_3N_4. In addition, the number of aromatic layers is also responsible for the orbital conjugation of g-C_3N_4 because of the partial overlap of p orbitals between the atoms in adjacent layers. Excessively high temperature gives rise to the separation of layers and the decomposition of single-layer networks, thus leads to the narrowed electron delocalization range of g-C_3N_4 and the concurrently widened band gap. It is worth noting that both CN-650 and CN-700 have two absorption edges. For example, the two absorption edges of CN-700 are located at about 412 nm and 646 nm, which area scribed to the π–π* transition and the n–π* transition, respectively. Fig. 2b displays the orbital energy levels of g-C_3N_4 at different conditions. It is well-known that organics with unsaturated heteroatomic groups have n electrons and π electrons. Electrons at n orbital can be excited to π* orbital by the light with a certain frequency, which is called the n–π* transition. Considering the molecular structure of g-C_3N_4, this n–π* transition would take place under light excitation. As can be seen in Fig. S4a,† for g-C_3N_4 with completely planarized layers, the n orbital of sp^2 N atom in a tri-*s*-triazine ring should be perpendicular to the p orbital of the neighboring N atom and direct to its nodal plane, there is no net bonding effect under this situation because the wave function

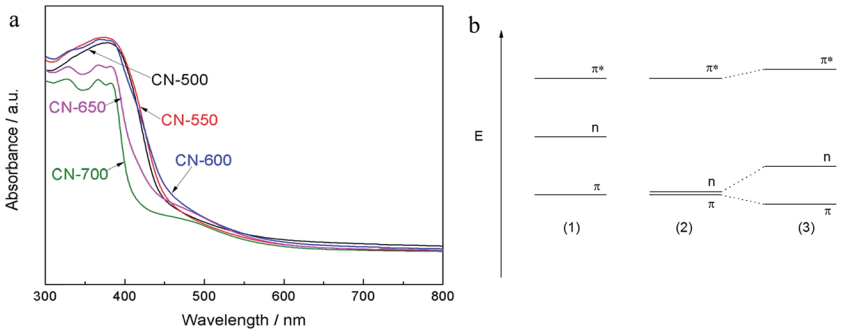

Fig. 2 (a) The UV-vis diffuse reflectance absorption spectra of g-C_3N_4 samples obtained at different temperatures; (b) the energy level of n, π, π* orbitals of g-C_3N_4 (1) with completely planarized structure, (2) obtained at relatively low temperature, (3) obtained at higher temperature.

of p orbital has the opposite sign. However, g-C_3N_4 is actually incompletely planarized, thus the n orbital and p orbital would generate effective overlap (Fig. S4b†), and the energy of n orbital could be lowered and approach to the energy of π orbital because of the net bonding effect between n orbital and p orbital. At relatively low temperature (500–600 °C), the planarization degree of g-C_3N_4 obtained is low, so the energy needed for π–π* and n–π* transition is very close and there is no detectable absorption edge which attributes to n–π* transition in UV-vis absorption spectra. Increasing the temperature leads to the improvement of planarization of g-C_3N_4, the narrowing of the effective overlap region between n orbital and p orbital and consequently the rising of the energy of n orbital. In addition, the thermal decomposition of g-C_3N_4 under higher temperature makes the energy of π orbital reduce. Therefore, g-C_3N_4 obtained at higher temperatures (650, 700 °C) shows obvious absorption edge ascribed to n–π* transition. In fact, the gradual emergence of n–π* transition with the increase of temperature can be also observed in the UV-vis spectra of melamine-derived g-C_3N_4 (Fig. S5†).

The surface area plays a very important role in the photocatalytic performance of semiconductors. As can be seen in Table S2,† the BET surface area of g-C_3N_4 increases with the polymerization temperature, which is in accordance with previous reports.[8,9] High temperature, on the one hand, gives rise to the separation of layers in g-C_3N_4, leading to the enhanced external surface area; and on the other hand, causes the decomposition of its layer networks, creating some additional pores in its structure.

The photoreduction activity of the obtained g-C_3N_4 was examined by H_2 production from water splitting under visible light irradiation (λ > 420 nm). Chloroplatinic acid was used as the precursor to create H_2 reduction sites (Pt nanoparticles) and triethanolamine was used as the electron donors. The results are summarized in Table S2.† As can be seen, the photocatalytic activity of the obtained g-C_3N_4 is enhanced with the increasing polymerization temperature, and CN-700 shows the best photoreduction performance with a H_2 evolution rate of 32.4 μmol h^{-1}, which is about 3.4 times higher than that of the g-C_3N_4 obtained from cyanamide. Furthermore, CN-700 also has excellent stability in H_2 evolution. As shown in Fig. 3a, H_2 has been produced steadily under the irradiation and there is no significant deactivation during 3 consecutive runs (12 h).

In addition to the superior photoreduction ability of the as-synthesized g-C_3N_4, a striking enhancement of photooxidation activity was also observed in the RhB photodegradation experiments. Fig. 3b shows the adsorption properties and photocatalytic activities of the g-C_3N_4 samples obtained at different temperatures. For comparison, the photodegradation behavior of g-C_3N_4 synthesized from cyanamide is also included. All the samples reach adsorption–desorption equilibrium within 60 min. The g-C_3N_4 samples obtained at higher temperatures have larger adsorption capacities, consistent with their larger BET surface areas (Table S2†). After irradiation with visible light, the

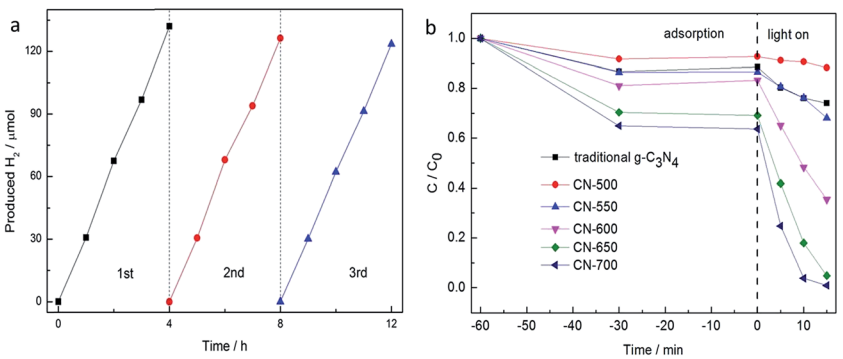

Fig. 3 Time course of (a) H_2 evolution for CN-700 and (b) RhB degradation for obtained g-C_3N_4 under visible light irradiation (λ > 420 nm).

RhB shows visible decomposition in the presence of all these samples. It should be mentioned that no reaction occurred when the system was illuminated in the absence of catalysts or in the presence of catalysts but without illumination. The photocatalytic activity of g-C_3N_4 is greatly enhanced by increasing polymerization temperature. CN-700 shows distinctively high degradation efficiency and it can completely decompose RhB within 15 min, 6 times faster than the traditional g-C_3N_4, which needs 90 min to thoroughly eliminate RhB.

The semiconductor photoexcitation is the key process triggering photoreactions and it is mainly associated with the band structure of semiconductors. The band gap (π–π^*) energy value of CN-700 was measured to be 3.01 eV, which determines that CN-700 is not capable of producing photogenerated carriers through the electron transition from π orbital to π^* orbital under visible light (λ > 420 nm). But visible light (λ > 420 nm) irradiation can excite the electron at n orbital to π^* unoccupied orbital. Fig. 4 depicts the electron transition process of CN-700 irradiated with visible light (λ > 420 nm). After an electron is excited, there is a hole left at n orbital. The electron at π orbital is then excited by visible light to fill up the hole at n orbital. Consequently, the hole generated at π orbital and the electron excited to π^* orbital trigger the photooxidation and photoreduction reactions, respectively.

It is well known that the photooxidation and photoreduction capabilities of semiconductors strongly depend on their potentials of valence band maximum (VBM) and conduction band minimum (CBM), respectively.[19] By performing the valence band X-ray photoelectron spectroscopy, the VBMs of CN-700 and the traditional g-C_3N_4 were estimated to be 2.38 eV and 2.27 eV (Fig. S6†), respectively. And their corresponding CBMs were calculated to be −0.63 eV and −0.43 eV, respectively, from the formula $E_g = E_v - E_c$. It has been reported that the VBM and CBM of traditional g-C_3N_4 are 1.57 V and −1.13 V *versus* NHE (Normal Hydrogen Electrode), respectively,[20] so the electronic potentials of the CN-700 could be determined (Fig. S7†). It is clear that the VBM and CBM of CN-700 are 0.11 V higher and 0.20 V lower than those of the traditional g-C_3N_4, respectively. Such a widened electron potential gap should be largely responsible for the enhanced photooxidation and photoreduction performances of CN-700, compared with the traditional g-C_3N_4.

The crystallinity of semiconductors plays a significant role in the separation and migration of photogenerated carriers. Higher crystallinity means fewer defects in the semiconductors. The defects operate as traps and recombination centers of photogenerated electrons and holes, resulting in the decrease of photocatalytic activity.[1] In addition, for g-C_3N_4, higher crystallinity means higher polymerization level and more expansive electron delocalization, which is also in favor of carrier migration in the horizontal direction. Fig. S8† gives the XRD patterns of traditional g-C_3N_4 and CN-700. It is clear that CN-700 has higher crystallinity. Moreover, from the vertical aspect, compared to the thicker ones of traditional g-C_3N_4 (Fig. S9†), thinner sheets of CN-700 decrease the distance photogenerated electrons and holes have to migrate to reach reaction sites on the surface, and thus lower the recombination probability of charge carriers. To further understand the photophysical behaviors of photoexcited charge carriers of traditional g-C_3N_4 and CN-700, the photoluminescence spectra and time-resolved fluorescence decay spectra were recorded. As shown in Fig. 5a, traditional g-C_3N_4 exhibit a typical band to band PL peak centered at *ca.* 470 nm, while for CN-700, except this kind of PL peak centered at *ca.* 450 nm, its PL spectrum shows an obvious 'shoulder' like peak centered at *ca.* 530 nm, which probably arises from the π^*–n emission. The weakened PL intensity of CN-700 suggests the decreased radiative recombination probability of its photo-induced charge carriers. Fig. 5b show the time-resolved fluorescence decay spectra of traditional g-C_3N_4 and CN-700. Both spectra decay exponentially and the fluorescence of CN-700 decays slower than that of traditional g-C_3N_4. Deconvolution of the fluorescence decay spectra of these two samples both gives three radiative lifetimes as listed in Table 1. In detail, the life time of short-lived charge carries is almost the same for both samples, but the proportion of short-lived ones of

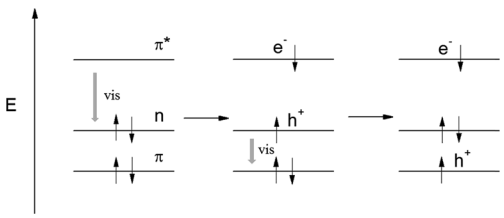

Fig. 4 Simplified electron transition process of CN-700 irradiated with visible light (λ > 420 nm).

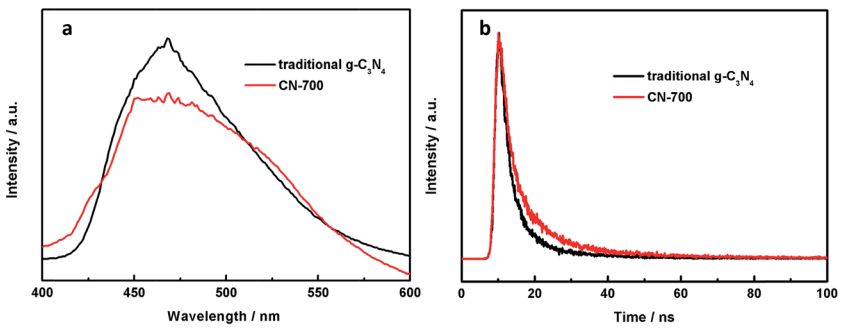

Fig. 5 Photoluminescence spectra (a) and time-resolved fluorescence decay spectra (b) of traditional g-C_3N_4 and CN-700.

Table 1 Radiative fluorescence lifetimes and their relative proportions of traditional g-C_3N_4 and CN-700

Sample	τ_1 (ns)–Rel%	τ_2 (ns)–Rel%	τ_3 (ns)–Rel%
Traditional g-C_3N_4	2.34–31.07	4.43–39.00	14.52–29.93
CN-700	2.41–19.94	8.22–49.99	33.53–30.08

CN-700 is much lower than that of traditional g-C_3N_4. From traditional g-C_3N_4 to CN-700, the life times of both medium-lived and long-lived charge carriers increase greatly, and their corresponding proportions also increase, especially the medium-lived charge carries. As for CN-700, the longer life times and larger proportions of medium and long-lived charge carries are certainly favorable for improving the probability of charge carries involved in photocatalytic reactions.[21] Furthermore, higher BET surface area of CN-700 (Table S2†) also makes contribution to its higher photocatalysis performance by endowing it with more active sites.

4. Conclusions

In summary, g-C_3N_4 photocatalyst with high thermal-stability has been successfully synthesized *via* the polymerization of cyanamide–urea solution. The textural property and electronic band structure of g-C_3N_4 can be optimized through elevating the polymerization temperature even to 700 °C. Because of the thermal decomposition at high temperature, the band gap of g-C_3N_4 is widened. Meanwhile, the energy level of n orbital of g-C_3N_4 is elevated. These changes activate the n–π* transition of g-C_3N_4 and help it absorb more visible light. The g-C_3N_4 obtained at 700 °C showed the highest photocatalytic activity among all the samples obtained. Compared with traditional g-C_3N_4 obtained from cyanamide, its photocatalytic H_2 evolution and RhB degradation efficiencies have been remarkably enhanced by 3.4 and 6.0 times under visible light, respectively, which can be attributed to its more competitive CBM or VBM potentials, higher crystallinity, thinner sheet morphology and higher BET surface area. The liberation of n electrons of g-C_3N_4 may be also beneficial for the improvement of its catalytic performance in base-catalyzed reactions (*e.g.* Knoevenagel reaction).

Acknowledgements

This work was financially supported by the National Key Basic Research Program of China (2013CB933200), National 863 plans projects (2012AA062703), National Natural Science Foundation of China (21177137) and the Key Program for Science and Technology Commission of Shanghai Municipality (11JC1413400).

References

1 A. Kudo and Y. Miseki, *Chem. Soc. Rev.*, 2009, **38**, 253–278.
2 A. Fujishima, T. N. Rao and D. A. Tryk, *J. Photochem. Photobiol., C*, 2000, **1**, 1–21.
3 X. Wang, K. Maeda, A. Thomas, K. Takanabe, G. Xin, J. M. Carlsson, K. Domen and M. Antonietti, *Nat. Mater.*, 2009, **8**, 76–80.
4 J. Zhang, G. Zhang, X. Chen, S. Lin, L. Mohlmann, G. Dolega, G. Lipner, M. Antonietti, S. Blechert and X. Wang, *Angew. Chem., Int. Ed.*, 2012, **51**, 3183–3187.
5 X. Wang, S. Blechert and M. Antonietti, *ACS Catal.*, 2012, **2**, 1596–1606.
6 B. Jürgens, E. Irran, J. Senker, P. Kroll, H. Müller and W. Schnick, *J. Am. Chem. Soc.*, 2003, **125**, 10288–10300.
7 J. Liu, T. Zhang, Z. Wang, G. Dawson and W. Chen, *J. Mater. Chem.*, 2011, **21**, 14398–14401.
8 F. Dong, L. Wu, Y. Sun, M. Fu, Z. Wu and S. C. Lee, *J. Mater. Chem.*, 2011, **21**, 15171–15174.
9 G. Zhang, J. Zhang, M. Zhang and X. Wang, *J. Mater. Chem.*, 2012, **22**, 8083–8091.
10 G. Liu, P. Niu, C. Sun, S. C. Smith, Z. Chen, G. Q. Lu and H. M. Cheng, *J. Am. Chem. Soc.*, 2010, **132**, 11642–11648.
11 P. Niu, L. Zhang, G. Liu and H. M. Cheng, *Adv. Funct. Mater.*, 2012, **22**, 4763–4770.
12 S. Yang, Y. Gong, J. Zhang, L. Zhan, L. Ma, Z. Fang, R. Vajtai, X. Wang and P. M. Ajayan, *Adv. Mater.*, 2013, **25**, 2452–2456.
13 P. M. Schaber, J. Colson, S. Higgins, D. Thielen, B. Anspach and J. Brauer, *Thermochim. Acta*, 2004, **424**, 131–142.
14 T. J. Prior, J. A. Armstrong, D. M. Benoit and K. L. Marshall, *CrystEngComm*, 2013, **15**, 5838–5843.
15 M. Shalom, S. Inal, C. Fettkenhauer, D. Neher and M. Antonietti, *J. Am. Chem. Soc.*, 2013, **135**, 7118–7121.
16 Y. Cui, J. Zhang, G. Zhang, J. Huang, P. Liu, M. Antonietti and X. Wang, *J. Mater. Chem.*, 2011, **21**, 13032–13039.
17 A. Thomas, A. Fischer, F. Goettmann, M. Antonietti, J. O. Muller, R. Schlogl and J. M. Carlsson, *J. Mater. Chem.*, 2008, **18**, 4893–4908.
18 S. C. Yan, Z. S. Li and Z. G. Zou, *Langmuir*, 2009, **25**, 10397–10401.
19 G. Liu, P. Niu, L. Yin and H. M. Cheng, *J. Am. Chem. Soc.*, 2012, **134**, 9070–9073.
20 Y. Zang, L. Li, Y. Zuo, H. Lin, G. Li and X. Guan, *RSC Adv.*, 2013, **3**, 13646–13650.
21 P. Niu, G. Liu and H. M. Cheng, *J. Phys. Chem. C*, 2012, **116**, 11013–11018.

